Acta Biomaterialia 105 (2020) 131–145

Contents lists available at ScienceDirect

Acta Biomaterialia

journal homepage: www.elsevier.com/locate/actbio

Full length article

Gelatin content governs hydration induced structural changes in silica-gelatin hybrid aerogels – Implications in drug delivery

Mónika Kéri[a], Attila Forgács[b,c], Vanda Papp[a,b], István Bányai[a], Péter Veres[b], Adél Len[d], Zoltán Dudás[e], István Fábián[b,c], József Kalmár[b,c,*]

[a] Department of Physical Chemistry, University of Debrecen, Egyetem tér 1, H-4032 Hungary
[b] Department of Inorganic and Analytical Chemistry, University of Debrecen, Egyetem tér 1, H-4032 Hungary
[c] MTA-DE Redox and Homogeneous Catalytic Reaction Mechanisms Research Group, Egyetem tér 1, H-4032 Hungary
[d] Nuclear Analysis and Radiography Department, Centre for Energy Research, Hungarian Academy of Sciences, Konkoly-Thege Miklós út 29-33, Budapest, H-1121 Hungary
[e] Neutron Spectroscopy Department, Wigner Research Centre for Physics, Hungarian Academy of Sciences, Konkoly-Thege Miklós út 29-33, Budapest, H-1121 Hungary

ARTICLE INFO

Article history:
Received 26 September 2019
Revised 22 December 2019
Accepted 10 January 2020
Available online 15 January 2020

Keywords:
Aerogel
Hydration
Mechanism of drug release
NMR spectroscopy
SANS

ABSTRACT

Silica-gelatin hybrid aerogels of varying gelatin content (from 4 wt.% to 24 wt.%) can be conveniently impregnated with hydrophobic active agents (e.g. ibuprofen, ketoprofen) in supercritical CO_2 and used as drug delivery systems. Contrast variation neutron scattering (SANS) experiments show the molecular level hybridization of the silica and the gelatin components of the aerogel carriers. The active agents are amorphous, and homogeneously dispersed in these porous, hybrid matrices. Importantly, both fast and retarded drug release can be achieved with silica-gelatin hybrid aerogels, and the kinetics of drug release is governed by the gelatin content of the carrier. In this paper, for the first time, a molecular level explanation is given for the strong correlation between the composition and the functionality of a family of aerogel based drug delivery systems. Characterization of the wet aerogels by SANS and by NMR diffusiometry, cryoporometry and relaxometry revealed that the different hydration mechanisms of the aerogels are responsible for the broad spectrum of release kinetics. Low-gelatin (4–11 wt.%) aerogels retain their open-porous structure in water, thus rapid matrix erosion dictates fast drug release from these carriers. In contrast to this, wet aerogels of high gelatin content (18–24 wt.%) show well pronounced hydrogel-like characteristics, and a wide gradual transition zone forms in the solid-liquid interface. The extensive swelling of the high-gelatin hybrid backbone results in the collapse of the open porous structure, that limits mass transport towards the release medium, resulting in slower, diffusion controlled drug release.

Statement of Significance

Developing new drug delivery systems is a key aspect of pharmaceutical research. Supercritically dried mesoporous aerogels are ideal carriers for small molecular weight drugs due to their open porous structures and large specific surface areas. Hybrid silica-gelatin aerogels can display both fast and retarded drug release properties based on the gelatin contents of their backbones. The structural characterization of the aerogels by SANS and by NMR diffusiometry, cryoporometry and relaxometry revealed that the different hydration mechanisms of the hybrid backbones are responsible for the broad spectrum of release kinetics. The molecular level understanding of the functionality of these hybrid inorganic-biopolymer drug delivery systems facilitates the realization of quality-by-design in this research field.

© 2020 Acta Materialia Inc. Published by Elsevier Ltd.
This is an open access article under the CC BY-NC-ND license.
(http://creativecommons.org/licenses/by-nc-nd/4.0/)

* Corresponding author at: University of Debrecen, Department of Inorganic and Analytical Chemistry, 1 Egyetem tér, H-4032 Debrecen, Hungary.
E-mail address: kalmar.jozsef@science.unideb.hu (J. Kalmár).

https://doi.org/10.1016/j.actbio.2020.01.016
1742-7061/© 2020 Acta Materialia Inc. Published by Elsevier Ltd. This is an open access article under the CC BY-NC-ND license.
(http://creativecommons.org/licenses/by-nc-nd/4.0/)

1. Introduction

There are only a handful of studies published in the literature that report the molecular-level investigation of the physico-chemical factors that govern the drug delivery properties of advanced materials [1–6]. Evidently, none of the available papers deal with the physico-chemical investigation of a promising platform of drug delivery devices: mesoporous aerogels.

A variety of novel mesoporous inorganic (silica) and biopolymer (polysaccharide and protein) aerogels have recently been prepared [7–12]. Aerogels dried under supercritical conditions are promising platforms for oral and pulmonary drug delivery applications [13–15]. Novel administration routes and other biomedical applications are also investigated [16–21]. Biocompatible aerogels are emerging vessels for musculoskeletal drug delivery [22].

It is well-established that these open mesoporous materials can efficiently be impregnated with active ingredients by adsorptive precipitation using supercritical CO_2. This technique yields the highest possible loadings, and also ensures that the active ingredients are conserved in their amorphous forms inside the porous carrier matrices [23–26]. Adsorptive precipitation also ensures the homogeneous distribution of the active ingredients inside the porous matrices, that is cooperatively dictated by the thermodynamics of the multilayer adsorption of the drug molecules on the inner pore walls, and the intimate conditions of the pressure-drop induced precipitation of the drugs from supercritical CO_2 [24,27,28]. In general, the rate of the release of the amorphous active ingredient from the carrier is significantly faster than the dissolution of the (micro)crystalline forms of the same drug. Furthermore, the total drug concentration is also elevated, because the solution is in equilibrium with the amorphous solid, and recrystallization is slow. Thus, this carrier strategy increases both the rate and the thermodynamic driving force of drug dissolution, which enhances bioavailability [18–20,24]. Remarkable solubility increase has also been achieved with fat soluble vitamins when loaded into aerogels [25,29].

In order to optimize the functionality of an aerogel based drug delivery system, it is necessary to develop feasible strategies for fine-tuning its release properties. One possibility is to modify the surface of the carrier and tune its hydrophilicity and/or hydrophobicity, which directly sets the strength of interaction of the drug with the backbone of the aerogel [21,30]. Preparing core-shell or coated aerogel carriers has been proved to be a straightforward strategy to achieve retarded release in the case of otherwise rapid release aerogel systems [20,31–33]. Coating silica-alginate hybrid aerogel with hydroxypropyl methylcellulose (HPMC) and Ca(II)-alginate results in ca. 3-times slower drug release compared to the uncoated aerogel [31]. The coating of silica aerogel with Eudragit introduces pH control. Compared to the uncoated silica aerogel carrier, the rate of drug release from the coated aerogel is ca. 5-times slower in pH = 1.0 HCl solution, but it is intact in pH = 7.2 PBS [20,33]. Another strategy for the optimization of carrier functionality is to implement aerogels of hybrid inorganic-organic backbones. The physico-chemical properties of these hybrids, and thus, their release properties can easily be tuned by changing the ratio of their constituents [14,32,34–37].

In our previous publications we have shown, that silica-gelatin hybrid aerogels of varying silica-gelatin ratios are versatile drug delivery systems [38–41]. These aerogels can be loaded with small molecular weight hydrophobic drugs (ibuprofen, ketoprofen, triflusal) up to 20 wt.% by adsorptive deposition from supercritical CO_2. The silica-gelatin platform can provide both rapid and sustained (retarded) release of active ingredients depending on the inorganic/organic ratio of the hybrid carrier matrix [40–42]. In general, the rate and mechanism of drug release from aerogels is governed by the following factors in aqueous media [1,3,42]. 1) Erosion and degradation of the carrier matrix. 2) Strength of the interaction between the drug molecules and the backbone of the carrier. 3) Hydration of the aerogel and the drug [43]. 4) Hydration induced deformation and/or swelling of the carrier matrix [3,40,44–46].

In a previous publication we reported the systematic investigation of the mechanism of release of ibuprofen and ketoprofen from silica aerogel and from silica-gelatin hybrid aerogel of minor (4 wt.%) gelatin content [40]. It has been established that the release of the drugs is about one order of magnitude faster from the hybrid aerogel of 4 wt.% content than from the parent silica aerogel. The goal of this preceding project was to understand the molecular mechanism of this effect. That study has revealed that *i*) the interaction of the drugs with the aerogel carriers is governed by their respective protonation states; *ii*) the aerogels degrade into d = 20–50 μm particles in water; *iii*) the porosity of the well-hydrated silica particles remains intact with open pores; and *iv*) the silica-gelatin hybrid aerogel of minor (4 wt.%) gelatin content behaves similarly to the parent silica aerogel under release conditions in all but one aspect, i.e. the hydration of the backbone is much more feasible due to the presence of gelatin. Thus, the remarkable increase in the drug release rate has been attributed to the more pronounced hydration of the hybrid silica-gelatin backbone compared to silica [40,47,48].

The biocompatibility of silica-gelatin aerogels has been tested in vitro against multiple cell lines by using the MTT assay and time-lapse vide-microscopy imaging. The hybrid aerogels proved to be non-cytotoxic in nature. Detailed results are given in our previous publications [38,39].

The present study systematically investigates and compares the mechanisms of drug release from a series of hybrid silica-gelatin aerogels of a wide range of gelatin content from 4 wt.% to 24 wt.%. Importantly, the carriers with low gelatin contents are rapid release systems, while aerogels with high gelatin content show sustained release properties. Dry aerogels are characterized by scanning electron microscopy (SEM), N_2 adsorption-desorption porosimetry and small-angle neutron scattering (SANS). The mechanism of wetting and hydration is investigated by non-conventional nuclear magnetic resonance (NMR) methods, such as cryoporometry, diffusiometry and relaxometry, complemented with SANS measurements. The structural information is correlated with high time-resolution release experiments, that are evaluated by appropriate mathematical models. Finally, clear conclusions are drawn between the compositions, structures and hydration properties of the aerogels and the kinetics and mechanism of drug release. A mechanism is established for the in-depth interpretation of the functionality of a systematically designed aerogel based drug delivery platform.

2. Experimental

2.1. Materials and solutions

Tetramethoxysilane (TMOS) was used as the silica precursor and it was obtained from Fluka. Food grade gelatin (Type A, 150 kDa) was purchased from Dr. Oetker, offering high purity and assured quality products. Methanol, acetone and ammonium carbonate ($(NH_4)_2CO_3$) were purchased from Fluka. Ibuprofen (IBU) [(RS)−2-(4-isobutylphenyl) propanoic acid] and ketoprofen (KET) [2-(3-benzoylphenyl) propanoic acid] were purchased from Sigma-Aldrich. Supercritical CO_2 was produced from 99.95% pure gas (Carburos Metalicos SA). All aqueous solutions were prepared with Milli-Q water (Millipore). Other chemicals (HCl, NaOH, NaH_2PO_4, cyclohexane and hexane) were ACS reagent grade (Sigma-Aldrich).

2.2. Preparation of aerogels

Silica-gelatin hybrid aerogel monoliths of varying gelatin content were synthesized by using a sol-gel process, as described previously [39–41]. Hybrid alcogels were produced by the co-gelation of gelatin and TMOS. After gelation, a multiple step solvent exchange protocol was carried out using pure acetone in the end. The gels were dried with supercritical CO_2 at 14 MPa and 80 °C using the medium pressure technique [49].

Previous results with silica-gelatin aerogels verified, that the total amount of gelatin is homogeneously incorporated into the aerogel backbone, forming a hybrid in each case [39–41]. The gelatin content of the hybrid aerogels was measured by thermal analysis to be 3.7, 11, 18 and 24 wt.%, respectively [39–41].

Hybrid aerogels of gelatin contents higher than ca. 25 wt.% were excluded from this study, because we experienced an elevated risk of formation of local inhomogeneities in the backbones, and such inhomogeneities often yield inconclusive materials properties.

2.3. Characterization of dry aerogels

Scanning electron microscopy (SEM) images were recorded on a Hitachi S-4300 instrument (Hitachi Ltd., Tokyo, Japan). Aerogel shards, freshly split from the monoliths were immobilized with superglue and Wood's metal, and covered by 5–6 atomic layer thick sputtered gold conductive layers. Typically, 15 kV accelerating voltage was used.

The specific surface area, the pore size distribution and the specific pore volume of the aerogels were measured by N_2 adsorption-desorption porosimetry (Quantachrome Nova 2000e). All samples were degassed at 80 °C for 24 h before the measurements. Specific surface area and pore size distribution were calculated using the standard protocols of multipoint BET and BJH methods, respectively.

2.4. Particle size of wet aerogels

The size distribution of aerogel particles was measured by using a hemocytometer and image analysis after wet grinding the samples by a Potter-Elvehjem tissue grinder (10 min) and sonication (5 min) [40,47]. Images were taken from c = 0.5 mg/mL suspensions with a 1.3 MP USB microscope camera. The ImageJ software was used for calculating the size distribution of the particles.

Additionally, the size distribution of aerogel particles was measured by laser diffraction light scattering (LDLS, MALVERN Mastersizer 2000) using conventional instrument setup and operation.

2.5. Zeta potential of aerogel particles

Aerogels were wet ground by a tissue grinder (see above), and the zeta potential was measured at a final aerogel concentration of 0.1 mg/mL on a MALVERN Zetasizer Nano ZS instrument using conventional instrument setup and operation. Zeta potential was measured between pH = 3.0 and pH = 7.4. The lower pH-limit of the Zeta cell is specified to be pH =3.0 by the manufacturer. The pH = 7.4 medium used here was the same PBS buffer that was used in the drug release experiments.

2.6. Nuclear Magnetic Resonance (NMR) methods

2.6.1. NMR cryoporometry

Water and cyclohexane were used as probe liquids. In each experiment ca. 70 mg dry, powdered aerogel was measured into a 5 mm wide glass NMR tube. The amount of the probe liquid was set to ca. 500 µL in order to fully saturate the pores of the aerogel, plus introduce a minor bulk phase. After homogenization, the wet samples were stored for 24 h at room temperature before NMR measurements.

Melting and freezing experiments were performed on a 360 MHz NMR instrument equipped with a 5 mm direct QNP probe head and on a 400 MHz NMR instrument with an inverse broadband probe head, both of which were cooled with dried air and BCU-05 and BSCU-05 cooling units. The Carr–Purcell–Meiboom–Gill (CPMG) spin-echo pulse sequence was applied to eliminate the broad signal of the solid phase during the echo time (1.5 ms for water and 10 ms for cyclohexane). Temperature was calibrated on glycol and methanol [50]. Experiments were always started with melting, and subsequent freezing and melting cycles were performed in the given temperature range. Spin-echo ^{1}H spectra were recorded in 0.2–0.3 K steps keeping the sample at constant temperature for 5 min before measurement. MestReNova 9.0 software was used for spectra post processing.

The melting and freezing point depressions of a liquid confined in a small space, and the shape of the corresponding melting-freezing hysteresis loop (determined by pore geometry) are given by the modified Gibbs-Thomson equations [51–53]. Model-free cryoporometry constants were applied (K_c = 30 nmK for water, 96 nmK for cyclohexane). Further details on data evaluation are given in the Supporting Information.

2.6.2. NMR diffusiometry

In each experiment ca. 70 mg dry, powdered aerogel was measured into a 5 mm wide glass NMR tube. The volume of added water was 100, 200 and 300 µL in different experiments, resulting in water / aerogel mass ratios of 1.3–4.3 g/g. The suspensions were mixed, sonicated, compacted by hand and stored for 24 h at room temperature before NMR measurements.

The self-diffusion coefficient of water in wet aerogel samples were measured with a stimulated spin echo pulse sequence using bipolar gradient pulses (BIPLED) to avoid eddy currents [54]. The experiments were performed on a Bruker Avance II 400 NMR spectrometer using the standard pulse program at 298 K. The length of the gradient pulse (δ) was set to 2–3 ms, while diffusion time (Δ) was varied between 10 and 120 ms in order to study its effect on the observed diffusion coefficient (D_{obs}). The gradient strength (G) was increased from 0 to 50 cm^{-1} Gauss in 32 square-equidistant steps. Spectra were transformed and evaluated with MestReNova 9.0. Diffusion data were evaluated according to the expression: [55–58]

$$I = I_0 \exp\left\{-D_{obs}\gamma^2(\Delta - \delta/3)\delta^2 G^2\right\} \quad (1)$$

When multiple diffusion domains are present in the sample each domain is represented by a different single-exponential function of a given D_{obs} value, and the observed decay is the sum of these functions [59,60]. In order to determine the number of diffusion domains, data were processed by inverse Laplace transformation (Multi-Exponential Relaxation Analysis, MERA) on the basis of the CONTIN method. Data were also fitted with single- and multi-exponential functions by using the Levenberg–Marquardt least-squares algorithm (OriginPro 8.6). The gradient was calibrated for D_2O to obtain the real diffusion coefficients [61].

2.6.3. NMR relaxometry

In the relaxometry experiments, the water / dry aerogel mass ratio was increased from 0 to 3.8 g/g in 12–15 steps. In each experiment ca. 100 mg dry, powdered aerogel was introduced into a 10 mm glass tube and an aliquot of water was added. The wet aerogel samples were mixed and sonicated. All samples were stored for 48 h at room temperature in sealed vessels to achieve complete equilibration before NMR measurements. Experiments were performed with the same sample wetted in multiple steps,

and with multiple samples wetted with different amounts of water. The results were identical within experimental error.

The measurement of T_2 transverse relaxation times was carried out on a 20 MHz Minispec Bruker mq20 relaxometer using the classical CPMG spin-echo pulse sequence. The echo time was varied between 80 and 300 μs, and the number of echoes was set to reach the total exponential decay of the signal. The relaxation delay was optimized according to the longitudinal relaxation time (T_1), determined previously using the inversion-recovery sequence. The lengths of the 90° pulse was determined for each sample, and varied between 1.6–2.1 μs with a pulse attenuation of 6 dB.

Water can be found in different relaxation domains in a sample. Each relaxation domain contributes to the measured signal by a single exponential decay, and the observed signal is the sum of these decays [55,62–66]. In order to determine the number of relaxation domains, data were transformed by inverse Laplace transformation (Multi-Exponential Relaxation Analysis, MERA) on the basis of the CONTIN method [67]. In line with the number of relaxation domains determined by MERA, primary data were fitted with a single- or a multi-exponential function by using the Levenberg–Marquardt least-squares algorithm (OriginPro 8.6). The T_2 transverse relaxation time and the amplitude were estimated for each domain.

2.7. Small Angle Neutron Scattering (SANS)

Dry, powdered aerogel samples were introduced into 2 mm-thick quartz cuvettes and measured without any pre-treatment. Some samples were wetted either with D_2O or with a 1:2 H_2O–D_2O mixture to a water / dry aerogel mass ratio of 3.3 g/g. After homogenization, the wet samples were stored overnight at room temperature before SANS measurements.

SANS experiments were performed on the Yellow Submarine instrument at Budapest Neutron centre. This is a pin-hole type instrument with a two dimensional neutron detector. Two sample-to-detector distances (1.2 m and 5.4 m) and two wavelengths (4.38 Å and 10.23 Å) were used. The beam diameter was 8 mm. Samples were measured for 60–180 min at room temperature. By modification of the wavelength and sample detector distance, a Q range of 0.008–0.4 $Å^{-1}$ was covered. The momentum transfer (Q) is defined by the following equation:

$$Q = \frac{4\pi}{\lambda}\sin\frac{\theta}{2} \tag{2}$$

where λ is the wavelength of the monochromatic neutron beam and Θ is the scattering angle. The definition of the scattering intensity (I) is as follows:

$$I(\lambda,\theta) = I_0(\lambda)\Delta\Omega\eta(\lambda)TV\frac{d\Sigma}{d\Omega}(Q) \tag{3}$$

where λ is the wavelength of the monochromatic neutron beam, Θ is the scattering angle, I_0 is the incoming neutron flux, $\Delta\Omega$ is the unit solid angle, $\eta(\lambda)$ is the detector efficiency, T and V are the transmission and volume of the sample and $\frac{d\Sigma}{d\Omega}(Q)$ is the macroscopic differential cross section. The macroscopic differential cross section conveys structural information on the studied system. The measured scattering intensity was corrected for sample transmission, empty cell scattering, solvent scattering, detector sensitivity and background scattering. The nano- and microstructural parameters of the scattering objects are determined from the mathematical analysis of the corrected $I(Q)$ curves.

For a wide Q range where both, the Guinier and the Porod approximations can be used for different parts of the SANS curve, the combination of both is valid. This is referred to as the Beaucage model, and it covers the whole Q range [68,69].

$$I(Q) \cong A\exp\left(-\frac{Q^2Rg^2}{3}\right) + B\left\{\frac{\left[\mathrm{erf}\left(\frac{QRg}{\sqrt{6}}\right)\right]^3}{Q}\right\}^{-p} \tag{4}$$

Rg is the average gyration radius, p is the Porod exponent, and A and B are coefficients related to the volume and number density of the scattering objects and to their contrast. Parameters A and B can be treated as adjustable scaling parameters.

Data fitting was performed by using least-squares algorithms in Igor Pro 6.1 software. Further details on the evaluation of SANS data are given in the Supporting Information.

2.8. Impregnation of aerogels

Dry, milled and sieved ($d_{particle}$ < 125 μm) aerogel powders were impregnated with ibuprofen and ketoprofen. The process was realized in an autoclave in supercritical CO_2 by utilizing the technique of adsorptive precipitation. Impregnation was performed at 45 °C and 20 MPa in a stirred reactor for 6 h. The depressurization rate was 0.2 MPa in order to avoid the crystallization of the drugs, as described previously [40,41]. Drug content was determined with RP-HPLC after soaking 5.0 mg loaded aerogel sample in 10.0 mL methanol for 2 h. The ibuprofen content of the loaded aerogels varies between 19 and 24 wt.%, and the ketoprofen content varies between 11 and 15 wt.%, as given in Tables S1 and S2 in the Supporting Information. The process of impregnation has been discussed previously [40,41].

The impregnated aerogel samples were characterized by X-ray diffraction (XRD) and infrared (FT-IR) spectroscopy methods. The results are in-line with previous, well-established observations, that the drugs are amorphous inside the hybrid aerogel carrier matrices [16,23,24,41].

2.9. Drug release tests

A custom built fiber optic UV–Vis spectrophotometer equipped with a fast CCD detector (AvaSpec-ULS-RS-TEC, Avantes) was used to monitor the dissolution of the active agents from the loaded aerogels [70]. Dry, loaded aerogel milled, and sieved to uniform size ($d_{particle}$ < 125 μm) was used in order to avoid any particle size-related effects. Loaded aerogel powder was weighted with 0.01 mg precision into a carefully dried spectrophotometric cuvette. The cuvette was thermostated at 37.0 ± 0.1 °C. On-line detection was started, and 3.0 mL pre-heated release medium (pH 2.0 HCl solution or pH 7.4 PBS) was introduced into the cuvette. The suspension was stirred at 300 rpm by a 2 × 8 mm PTFE coated magnetic stir-bar. The detector was typically operated with 30 ms integration time and 20 subsequent spectra were averaged. Absorbance change was followed in the 200–800 nm wavelength range in 1.0 nm steps for at least 1000s with a minimum time resolution of 1.0 s. As the drug dissolved from the aerogel, the characteristic absorbance signal of either IBU or KET was detected in the suspension [9,40]. It is important to note, that the light scattering of the aerogel suspension was taken into correction by subtracting it from each recorded spectrum using the “dual-wavelength method” developed by Liu and Zhu [71,72]. The published protocols were implemented without any alterations. As a verification method, drug release was also followed by HPLC for sustained release systems. The final concentration of the drug was additionally measured in every experiment by HPLC by using a method described in our previous publication [41]. For each sample, cumulative drug release is given as the percentage of the total amount of loaded drug in the aerogel. The detailed conditions of the drug

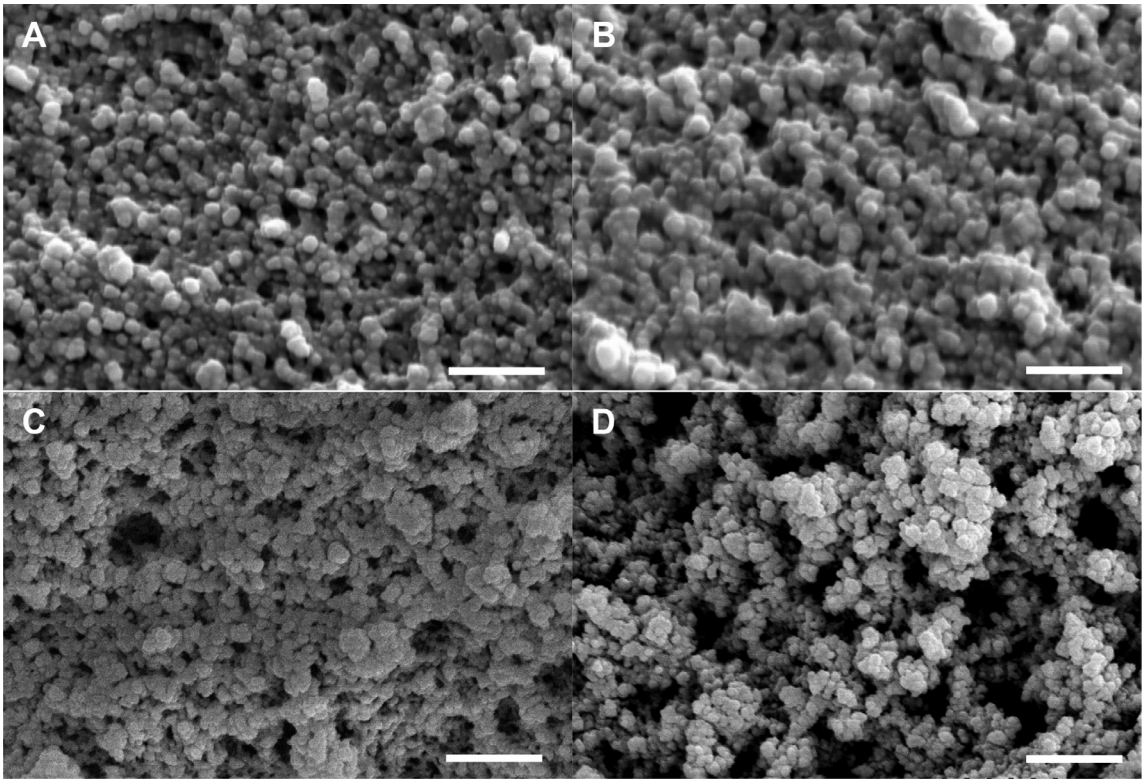

Fig. 1. Scanning electron micrographs (SEM) of a pristine silica aerogel (A) and silica-gelatin hybrid aerogels of 4 wt.% (B), 11 wt.% (C) and 24 wt.% (D) gelatin content. All scale bars represent 1.0 μm.

release tests are listed in Tables S1 and S2 in the Supporting Information. For comparison, the solubilities of the amorphous forms of IBU and KET are also given in Tables S1 and S2. All experiments were performed in 3 replicates.

Kinetic model fitting was performed based on well-established theories by using a robust non-linear Levenberg-Marquardt least-squares algorithm, as described earlier [73].

3. Results and discussion

3.1. Morphology and pore structure of dry aerogels

3.1.1. Scanning electron microscopy

Micrographs of silica and silica-gelatin aerogels are shown in Fig. 1 in 25k × magnification. All studied aerogels are built from primary spherical blocks, that is archetypical to silica aerogels. The size of these blocks is in the range of d_{sphere} = 50 – 100 nm, and this size is independent of the gelatin content of the network. The fundamental morphology of the hybrids is uniform, and it is similar to that of pure silica aerogels. However, both the number and the size of macrospores increase systematically with increasing gelatin content. Thread-like motifs are also visible for aerogels with 24 wt.% gelatin. These findings suggest systematic structural changes in the hybrids due to the incorporation of gelatin into the silica network.

3.1.2. N_2 adsorption-desorption porosimetry

Representative N_2 adsorption-desorption isotherms are shown in Fig. 2A for dry silica and silica-gelatin aerogels. All of the experimental hysteresis curves are IUPAC type IV (H2), which is characteristic for mesoporous materials. The steep rise of the isotherms at $p/p_0 = 1$ indicates the presence of macropores [74]. The specific surface area (S_{BET}) of the hybrid aerogels is between 799 m^2 g^{-1} and 285 m^2 g^{-1} and it systematically decreases with increasing gelatin content (Table 1). The pore size distribution curves of the aerogels calculated by the BJH method are shown in Fig. 2B. In order to highlight the differences between the distribution curves, the x-axis is shown on the normal scale, and not on the logarithmic scale. The pore size distribution is wider and the contribution of the larger pores is more significant at higher gelatin content. The total specific pore volume (V_p) corresponding to d_{pore} < 200 nm systematically decreases with increasing gelatin content (Table 1). Unfortunately, pores larger than 200 nm are excluded from the N_2 porosimetry analysis, as a consequence of the working principle of the technique. Thus, the V_p value is representative only when the macropore contribution is small. This is further discussed in connection with NMR cryoporometry in Section 3.2.3.

Table 1
Textural properties of silica and silica-gelatin hybrid aerogels derived from N_2 gas adsorption-desorption porosimetry data (cf. Fig. 2). Mean ± SD values represent 3 replicate measurements.

	S_{BET} (m^2/g)[a]	V_p (cm^3/g)[b]	d_{pore} (nm)[c]	*C*-constant
silica	812 ± 61	6.20 (198 nm)	32	89
4 wt.% gelatin	799 ± 72	4.95 (161 nm)	25	73
11 wt.% gelatin	627 ± 60	4.48 (205 nm)	32	92
18 wt.% gelatin	416 ± 46	2.31 (213 nm)	17	87
24 wt.% gelatin	285 ± 32	1.69 (194 nm)	20	85

[a] BET specific surface area.
[b] Total specific pore volume (upper threshold of pore diameter included in the calculation).
[c] Mean pore diameter: estimated at the maximum of the distribution curve.

According to the combined SEM and N_2 porosimetry results, the contribution of macropores is significant at high (18–24 wt.%) gelatin contents. The increasing amount of incorporated gelatin in the backbone results in the opening and loosening of the dry aerogel matrix. The contribution of micropores was estimated for each aerogel by using the *t*-plot method, based on the de Boer model

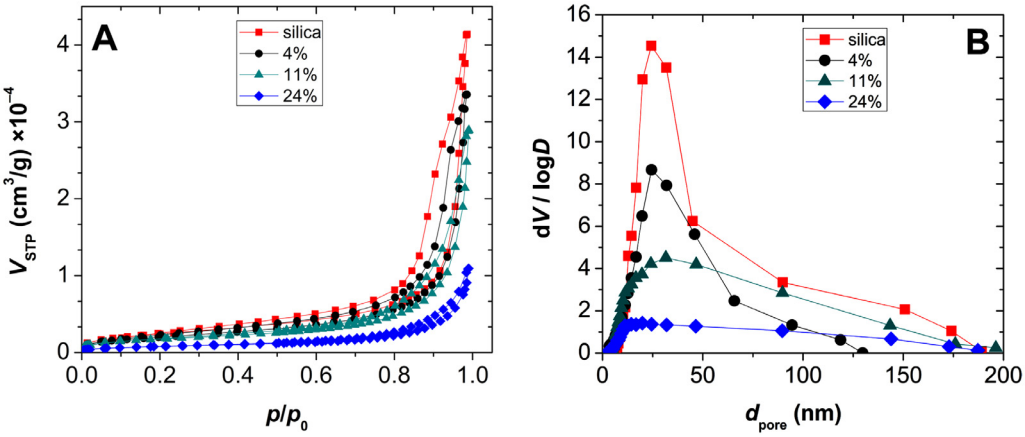

Fig. 2. Nitrogen adsorption-desorption isotherms (A) and BJH pore size distribution curves (B) of silica and silica-gelatin hybrid aerogels of different gelatin content (given in the legend as wt.%).

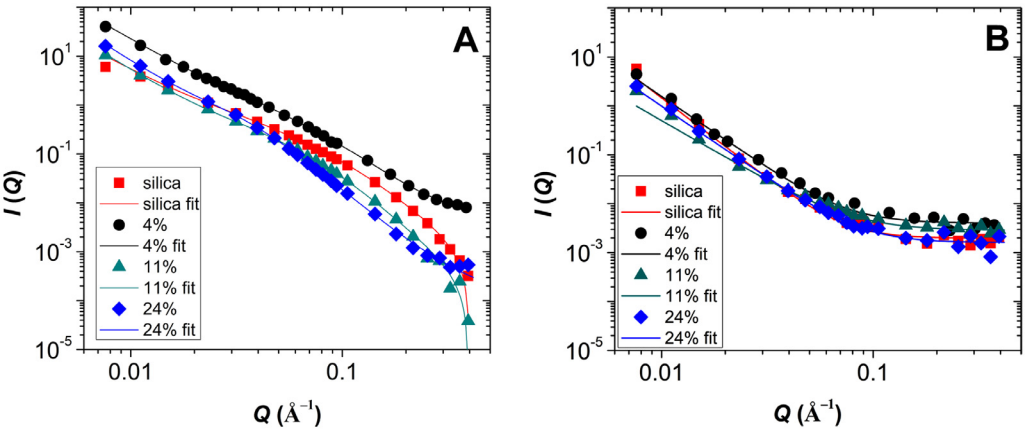

Fig. 3. Small angle neutron scattering (SANS) curves of silica and silica-gelatin hybrid aerogels measured in their dry states (A) and when completely hydrated (B) by 1:2 H_2O:D_2O mixture (3.3 g liquid / g dry aerogel). Solid lines represent data fitting to the Beaucage model (Eq. (4)). Estimated structural parameters for the dry aerogels are given in Table 2. (For interpretation of the references to colour in this figure legend, the reader is referred to the web version of this article.)

of statistical thickness [75]. The results indicate that there are no pores present below $d_{pore} = 2$ nm in any of the aerogels.

3.1.3. Morphology of dry aerogels by SANS

Nanometer sized material inhomogeneities (scattering objects) that have neutron scattering length densities different from their surroundings yield meaningful SANS curves. These scattering curves carry information on the size, spatial distribution, shape and surface morphology of the scattering objects. The primary difference in neutron scattering length densities in dry mesoporous aerogels, i.e. the contrast, is between the solid backbone and the air filled pores [52,76,77]. In the case of hybrid materials, the different components of the backbone can also give distinct contrasts.

Small angle neutron scattering curves measured for dry silica and silica-gelatin aerogels are shown in Fig. 3A. All of these curves can be adequately fitted with the Beaucage model (Eq. (4)). The average gyration radius (R_g) and the Porod exponent (p) were estimated for all dry aerogels (Table 2). The value of the Porod exponents are between 3 and 4 for silica aerogel and for hybrids of low gelatin content (4 wt.%). Such Porod exponents are characteristic for surface fractals. The value of the Porod exponent is ca. 4 for hybrid aerogels with moderate and high gelatin content (11 wt.%–24 wt.%), meaning that the boundary between objects of different contrasts is sharp and smooth [69]. This can be attributed to the high number of macropores. For macropores, the area of the pore walls is high and their apparent curvature is low compared to micropores and small mesopores. In line with this explanation, the gyration radius is the highest in the case of the aerogel with the highest gelatin content. Thus, the results of the SANS measurements are in excellent agreement with those of the SEM and the N_2 porosimetry.

Table 2
Values of the Gyration radius (R_g) and the Porod exponent (p) of dry and hydrated silica and silica-gelatin aerogel samples. Structural parameters were estimated by fitting small angle neutron scattering (SANS) curves (cf. Figs. 3A and 9) with the Beaucage model (Eq. (4)).

	dry	hydrated (D_2O)
silica	R_g = 36.8 Å	R_g = 31.9 Å
	p = 3.28	p = 3.87
4 wt.%	R_g = 37.3 Å	R_g = 30.3 Å
gelatin	p = 3.44	p = 3.97
11 wt.%	R_g = 36.4 Å	R_g = 28.2 Å
gelatin	p = 3.98	p = 5.15
24 wt.%	R_g = 54.0 Å	R_g: N/A
gelatin	p = 4.22	p = 2.71

3.1.4. Homogeneity of the hybrid backbone by SANS

The primary experimental observation is that the scattering curves of the dry silica and silica-gelatin aerogels do not show distinct features, i.e. there is no secondary contrast in the case of the hybrid materials. The simplest explanation for this phenomenon is to assume that there is no spatial heterogeneity in the solid silica-gelatin backbones [78]. In other words, the hybrid backbones scat-

ter as homogeneous materials, and contrast is the sole result of porosity.

In order to verify this theory, contrast-variation SANS experiments were performed. Silica and silica-gelatin aerogels were hydrated (3.3 g liquid / g aerogel) with 1:2 H_2O:D_2O mixture. The scattering length density of this mixture is ca. equivalent with that of silica [77]. Thus, the resulting scattering curve of hydrated silica aerogel is practically equivalent to the background. Interestingly, almost identical, uninformative scattering was measured for the hydrated hybrid aerogels as well, regardless of their gelatin content (Fig. 3B). The most feasible explanation is that the contrast of the silica-gelatin matrix approximately matches that of the pure silica. This is a strong indication that the hybridization of the silica-gelatin backbone is homogeneous at the molecular level, i.e. gelatin does not form a "layer" on pure silica, or shows any spatial preference [78].

3.2. Pore structure and morphology of hydrated aerogels

Water readily interacts with both silica and silica-gelatin aerogels. Two concerted processes take place. The solid backbone is hydrated, and in the same time, the monolithic structure partially disintegrates to yield microparticles [40,47]. Hydration can take different extents based on the composition of the aerogel backbone, which can lead to the alteration of the morphology and the pore structure of the wet aerogel. The disintegration of the aerogel monoliths is the result of breaking the bonds between the primary building blocks in the solid network due to the surface tension of water and minor hydrolytic reactions. As a result of the two coupled processes, aerogel microparticles form in water. The pore network of these wet particles either retains the original structure of the dry solids, or gets distorted due to the extensive hydration of the backbone.

The kinetics of hydration of the silica and silica-gelatin aerogels is fast, and complete in a few seconds when the solid matrices are flooded with water.

3.2.1. Particle size of hydrated aerogels

Particle size distribution of silica and silica-gelatin aerogels were measured after wet grinding the samples using a standardized protocol (cf. Section 2.4.). This protocol ensures that the difference in particle size is exclusively due to the different composition of the aerogels, which in turn governs their hydration and degradation. Size distribution curves measured by image analysis of micrographs and by laser diffraction light scattering (LDLS) agree well; the maximum difference in peak position is 12% among parallel measurements.

Both the position of the maximum and the width of the particle size distribution curve decrease systematically by increasing gelatin content (Fig. 4). In hybrid aerogels, the covalent silica network is disrupted by the incorporation of gelatin protein molecules that are bound to each other only by weak secondary forces. These secondary bonds easily break upon the hydration of the backbone. Thus, high gelatin content facilitates the degradation of the aerogel monoliths as a consequence of the facile hydration of the protein molecules.

3.2.2. Zeta potential of aerogel particles

Besides the size of the hydrated aerogel microparticles, their charge has a fundamental influence on the drug delivery properties, as well, because it controls the strength of the interactions between the aerogel backbone and the drug molecules.

The zeta potential (E_Z) of hybrid aerogel particles was measured between pH = 3.0 and pH = 7.4 (Fig. 5). The zeta potential of silica aerogel is +6 ± 1 mV at pH = 3.0, and −28 ± 2 at pH = 7.4. The isoelectric point of silica is at ca. pH = 3.5, which is in good

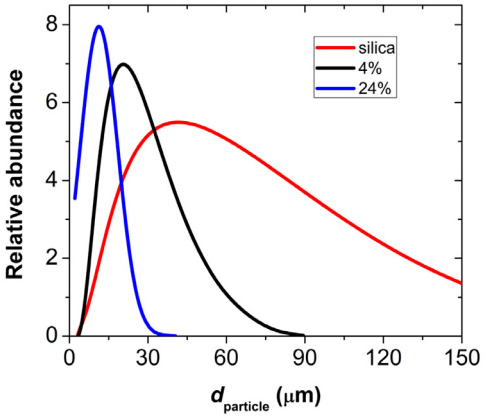

Fig. 4. Particle size distribution of wet silica and silica-gelatin hybrid aerogel particles measured by laser diffraction light scattering (LDLS). (For interpretation of the references to colour in this figure legend, the reader is referred to the web version of this article.)

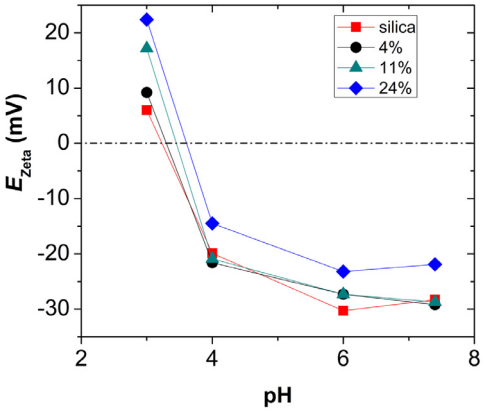

Fig. 5. Zeta potential (E_Z) of silica and silica-gelatin aerogel microparticles as function of pH.

agreement with previously reported values [79]. The zeta potential of the hybrid aerogels systematically increases with their increasing gelatin content at all pH values. The proportionality between E_Z and gelatin content is well-expressed at acidic pH (positive E_Z values), but not at neutral pH (negative E_Z values). The hybrid of 24 wt.% gelatin has a maximum E_Z of +22 ± 3 mV at pH = 3.0 and −22 ± 2 mV at pH = 7.4. The isoelectric point of aqueous Type A gelatin is reported to be at ca. pH = 5.5 [80], that is consistent with the present results.

3.2.3. NMR cryoporometry

The theory and application of NMR cryoporometry are discussed in detail by Strange et al., Petrov and Furó [51,52]. The primary information in NMR cryoporometry is the melting and freezing point depressions of probe liquid droplets confined inside micro-, meso– and/or macroporous solid networks. This information can be translated to droplet size distribution, which is equivalent to pore size distribution when the liquid completely fills the pores of the network [53]. In this case, the dominating shape of the pores is also reflected in the primary melting – freezing hysteresis curves.

First, NMR cryoporometry measurements were conducted with wet silica and silica-gelatin aerogels containing enough water to completely fill their pores. In the case of the silica aerogel, the cryoporometry curves indicate that the pore structure of the hydrated aerogel is nearly identical to that of the dry gel. The calculated pore size distribution is almost in complete agreement with

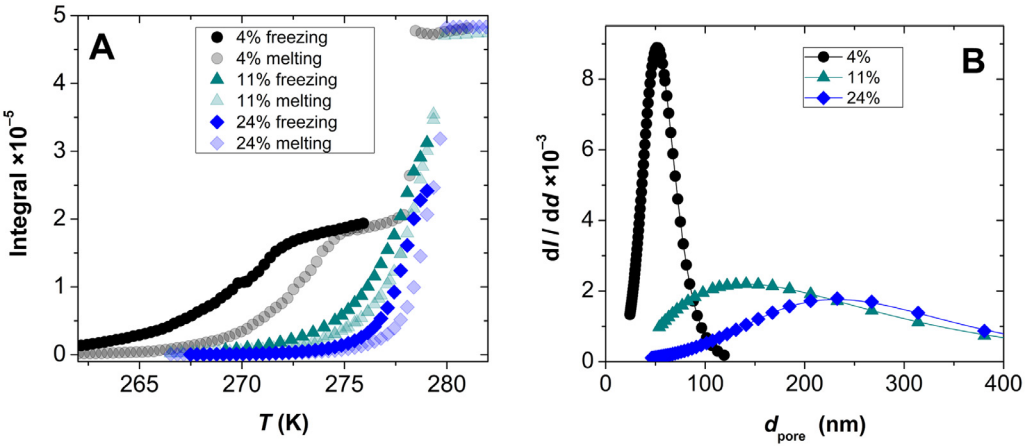

Fig. 6. NMR cryoporometry of silica-gelatin hybrid aerogels in cyclohexane. The filling of the pores is complete, and the amount of the bulk-liquid and the pore-liquid is ca. equivalent. Panel A: melting – freezing hysteresis curves. Panel B: Volume equivalent pore size-distribution curves calculated from the data in panel A. The calculation is based on the modified Gibbs-Thomson equations.

the one measured by N_2 porosimetry in the dry state [40,47]. The general conclusion is that during the hydration of silica aerogels, the monoliths disintegrate into microparticles (cf. Fig. 4), but the silica network and the pore structure of the microparticles remain intact, at the same time they are filled with water [40,47].

Interestingly, no meaningful NMR cryoporometry curves could be recorded for fully hydrated silica-gelatin hybrid aerogels, regardless of their gelatin content. A melting – freezing hysteresis loop was present in the case of the aerogel with the lowest (4 wt.%) gelatin content, but well-expressed steps were absent [40,47]. In the case of the hybrids with higher gelatin content, practically no melting and freezing point depressions were detected. This can be attributed to the strong hydration of the hybrid backbone which alters the pore structure and yields a hydrogel-like matrix [81]. Unfortunately, the extent of the alteration of the pore network compared to the dry state cannot be deduced from these cryoporometry measurements.

In order to prove that the observed collapse of the pore network can be exclusively attributed to the hydration of the hybrid aerogels, another probe liquid was implemented for cryoporometry [81]. Cyclohexane is a liquid that well solvates both silica and gelatin, and it is a widely used probe for cryoporometry. Representative melting – freezing curves and corresponding pore size distribution plots are shown in Fig. 6. The 1:2 ratio appearance of the melting – freezing hysteresis suggests the dominating presence of spherical pores in all aerogels [51]. The pore size distribution curves calculated from cyclohexane NMR cryoporometry are in excellent agreement with those measured by N_2 porosimetry for the dry aerogels (cf. Figs. 2B and 6B). This means that the pore structures of the dry aerogels are preserved upon solvation by cyclohexane. The mesopore and the macropore contributions were calculated from the size distribution curves in Fig. 6B. Total specific pore volume (V_p^{NMR}) was calculated from the primary NMR cryoporometry data, specifically from the height of the step associated with the freezing/melting process (see integral values in Fig. 6A). The ratio of the height of this step and the maximum integral value measured at the complete melting of the probe liquid is directly proportional to the ratio of the liquid filling the pores and the total liquid content of the sample. This calculation method is described in our earlier publication [40]. The estimated structural parameters are given in Table 3 for each silica-gelatin aerogel. The results support the conclusions drawn from the evaluation of the SEM pictures and the N_2 porosimetry data for the dry aerogels, i.e. macropore contribution significantly increases with the increasing gelatin content of the hybrid aerogels. Importantly, the estimated specific pore volumes (V_p^{NMR}) of the silica-gelatin aerogels are approximately the same regardless of their gelatin content. This is only an apparent contradiction with the N_2 porosimetry data, where V_p decreases with increasing gelatin content (cf. Table 1). Unfortunately, the V_p value is not representative when the macropore contribution is high, because pores larger than 200 nm are excluded from the N_2 porosimetry analysis. Thus, it is more realistic to accept the V_p^{NMR} values measured in cyclohexane to represent the specific pore volumes of the pristine silica-gelatin aerogels.

Table 3
Structural parameters of silica-gelatin hybrid aerogels estimated from primary and derived NMR cryoporometry data (cf. Fig. 6).

	V_p^{NMR} (cm³/g)[a]	%mesopore[b]	%macropore[b]
4 wt.% gelatin	3.4 ± 0.5	38	62
11 wt.% gelatin	4.5 ± 0.5	< 10	> 90
24 wt.% gelatin	4.3 ± 0.5	< 10	> 90

[a] Total specific pore volume.
[b] Cumulative volume equivalent mesopore and macropore contributions derived from pore size distribution.

As a summary, NMR cryoporometry measurements verify the presence of a strong, specific interaction between water and silica-gelatin hybrid aerogels. This interaction results in such alterations and distortions of the pore networks that do not take place in other solvents.

3.2.4. NMR diffusiometry

The observed self-diffusion coefficient (D_{obs}) of a liquid is altered compared to the bulk phase, when the liquid is confined in the pores of a solid network. The apparent self-diffusion coefficient is not independent of the length of the observation time of the diffusion experiment (Δ) in confinement. At limiting-short observation times, the molecules travel shorter distances than the size of the pores and do not collide with walls. In this case, the observed self-diffusion coefficient is equivalent to that of measured in the bulk phase [59,60]. At longer observation times, collisions with the walls reduce the effective distance covered by the molecules, and the apparent self-diffusion coefficient is lowered. Therefore, a sufficiently high observation time should be chosen if the goal of diffusiometry is to obtain information on the confinement of the liquid and on the permeability of the solid network [55–58,60].

It is possible that water is found in multiple diffusion domains (e.g. in the primary hydration sphere and as a bulk phase) in the

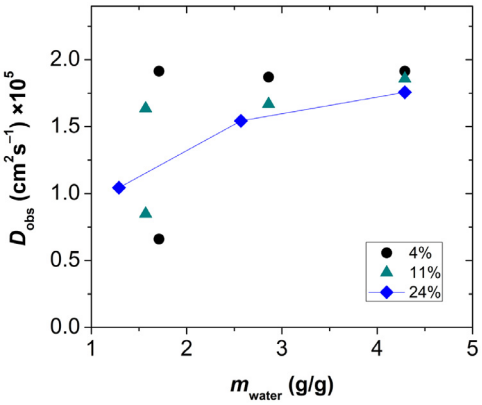

Fig. 7. NMR diffusiometry of hydrated silica-gelatin hybrid aerogels. Two diffusion domains are present in aerogels of lower gelatin content (4–11 wt.%) at low water content (< 2.0 g/g), and this is reduced to 1 diffusion domain at high water content. Only one diffusion domain is present in the hydrated 24 wt.% gelatin aerogel, regardless of its water content. (For interpretation of the references to colour in this figure legend, the reader is referred to the web version of this article.)

same sample. If water molecules in the different domains exchange slowly with each other on the timescale of diffusiometry, more than one apparent self-diffusion coefficients are measured for the same sample [55–58].

When the pores of silica aerogel are completely filled with water, only one characteristic diffusion domain is present [47]. The value of the single observed self-diffusion coefficient is set by the ratio of confined water in the pores and bulk water. This indicates that *i*) the primary hydration sphere of the silica network is not large enough to form an independent diffusion domain in the sample, and *ii*) the interchange of water in the pores and in the bulk phase is facile. Accordingly, the pore network of hydrated silica aerogel is open and permeable [47].

The apparent self-diffusion coefficient of water (D_{obs}) in hydrated silica-gelatin aerogels was measured by PGSE NMR experiments. The effect of 2 variables was tested: *i*) the water content of the hybrid aerogel samples, and *ii*) the observation time of the diffusion experiments [82,83]. First, it was established that the D_{obs} values are independent of the observation time at $\Delta \geq 40$ ms in all hydrated silica-gelatin aerogels (cf. Fig. S1 in the Supporting Information). Thereafter, the water content of each sample was varied and its effect on D_{obs} was deduced by using high observation times for the measurements.

Two diffusion domains were detected for aerogels of lower gelatin content (4–11 wt.%) at water contents below 2.0 g/g (Figs. 7 and S1). The slower diffusion domain is characteristic for water molecules in the primary hydration sphere of the hybrid backbone, [48] while the faster domain represents water molecules moving more freely inside the pores. The 2 domains are in slow exchange with each other, and the slower diffusion domain vanishes when the water content of the sample is increased. After the saturation of the hydration sphere, most of the water diffuses in the pores and this phase dominates the NMR signal. Interestingly, only 1 diffusion domain is present in the hydrated 24 wt.% gelatin aerogel, regardless of the water content of the sample (Figs. 7 and S1). This single D_{obs} value systematically increases with increasing water content, corresponding to a less and less compact non-porous structure. Hydrogels typically show this behavior [84]. Finally, at high water content, all hydrated silica-gelatin aerogels display approximately the same, single apparent self-diffusion coefficient for water, independently of the gelatin content of the matrix (Fig. 7). The highest observed self-diffusion coefficient of water is ca. 2.0×10^{-5} cm^{2}s^{-1} in the aerogel samples, while that is 2.3×10^{-5} cm^{2}s^{-1} in the pure bulk phase at 25 °C [61].

These results indicate, that hybrid aerogels with lower gelatin content retain a more or less permeable pore structure when treated with water, but hydrated 24 wt.% gelatin aerogel attains hydrogel-like characteristics even at low water content.

3.2.5. NMR relaxometry

The theory for interpreting ^{1}H NMR relaxation data used to describe the wetting mechanisms of porous solids is adopted from prior literature [62,63,65,67]. The relaxation rates of protons in water molecules heavily depend on the localization and the environment of the molecules in the sample. Generally, water molecules in the hydration sphere (adsorption layer) of a solid matrix and molecules confined in small pores relax faster than water molecules in the bulk liquid. The wetting mechanism of a porous solid can be deduced by titrating it with water and measuring the T_2 relaxation time as function of the water content of the sample [55,62,63,65].

In the case of hydrophilic porous solids, water molecules first adsorb on the surface forming mono- and multilayers. Water adsorbed on a hydrophilic surface is characterized by a short transverse relaxation time (T_{2s}) compared to bulk water (T_{2b}). When molecules in these 2 domains exchange on the timescale of relaxometry, the observed T_2 relaxation time can be given as the combination of the 2 limiting relaxation times:

$$\frac{1}{T_2} = \frac{V_s}{V_0} \times \frac{1}{T_{2s}} + \frac{V_b}{V_0} \times \frac{1}{T_{2b}} \quad (5)$$

where V_0 is the total volume of water in the sample, V_s and V_b are the volumes of water on the surface and in the bulk phase, respectively ($V_0 = V_s + V_b$), and T_2 is the observed transverse relaxation time.

When the amount of water is increased in the solid sample, the filling ratio of the pores is higher. At higher filling ratios, multiple quasi-bulk regions (puddles) can form atop the primary water layer, e.g. in the corners of concave pores. If these puddles are large, the exchange of water molecules between the quasi-bulk phase and the primary layer can be slow enough for the observation of multiple T_2 relaxation times [67]. Multiple relaxation times can also be observed when water is located in spatially separated spots in the porous matrix. An example is a mixed micro- and mesoporous matrix that has well separated micropores. These micropores can be filled before the mesopores, and small bottlenecks can hinder the exchange of water among different pores at moderate filling ratios. However, the spatial separation of water is uncommon in highly hydrophilic porous solids, because thermodynamic preferences dictate the formation of a thick, continuous water layer throughout the network [85].

In the present study, relaxometry was performed with hydrated silica and silica-gelatin aerogels of different water content (i.e. at different filling ratios). Inverse Laplace transformation of primary data shows the presence of only one water relaxation domain in both the silica and the hybrid samples until a mass ratio of 0.5 g water / g dry aerogel. At higher water contents, 2 relaxation domains are present in all samples, as seen in Fig 8. (Inverse Laplace plots are shown Fig. S2 in the Supporting Information). In accordance with the classical theory, we propose that the faster relaxation domain represents the hydration sphere of the aerogel backbone, and the slower relaxation domain represents water situated farther from the pore walls, e.g. in puddles forming in focal points of the aerogel network.

For the quantitative evaluation of the relaxometry data of wet aerogels, first, the measured T_2 relaxation times are plotted as function of water content (Fig. 8A), and second, the reciprocal value of T_2 is plotted as function of the reciprocal value of filling factor f (Fig. 8B). The total specific pore volumes of the wet aerogels, representing the unity filling factor ($f = 1$), were esti-

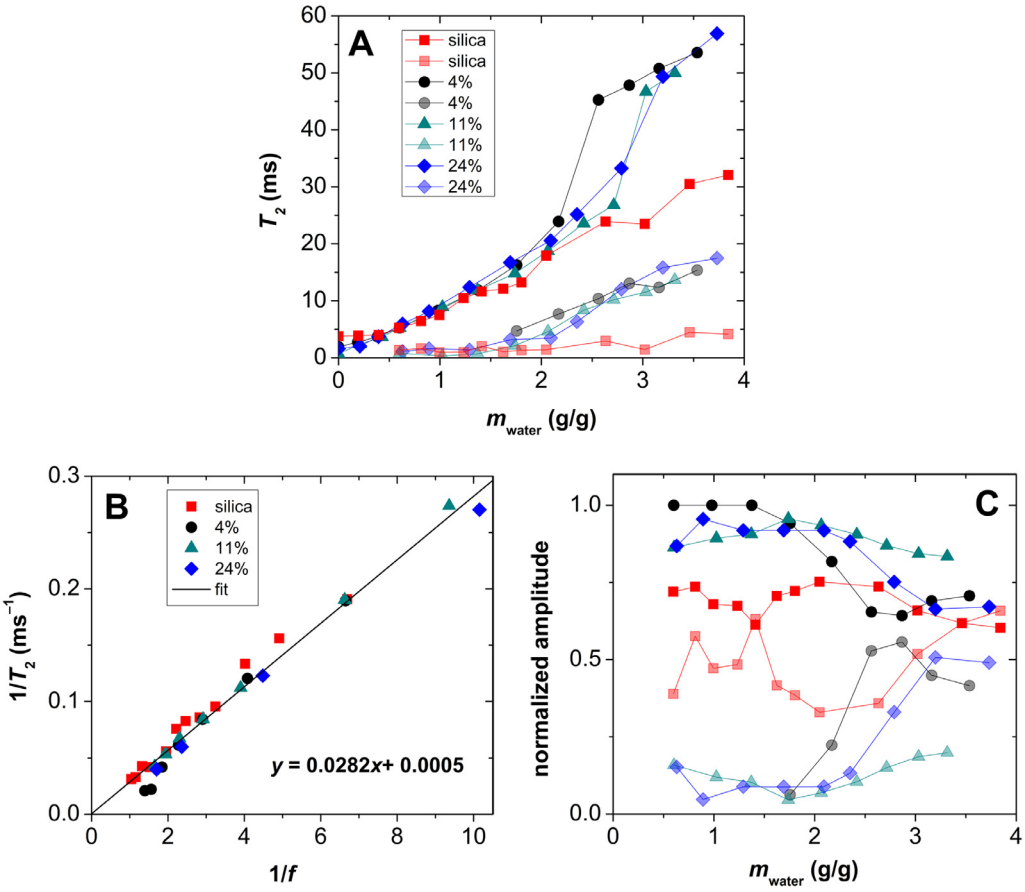

Fig. 8. NMR relaxometry of hydrated silica and silica-gelatin hybrid aerogels. Two relaxation domains are present for each aerogel at mass ratios higher than 0.5 g water / g aerogel. Panel A: measured T_2 relaxation times as function of water content. Panel B: reciprocal T_2 as function of reciprocal filling factor (f) for the fast relaxation domain. Panel C: normalized amplitude of each relaxation domain (cf. panel A). (For interpretation of the references to colour in this figure legend, the reader is referred to the web version of this article.)

mated from NMR cryoporometry data and are referred to as V_p^{NMR} (Table 3). Therefore, the filling factor was calculated versus ca. 4.0 cm^3/g total specific pore volume ($f = 1$) for all aerogels. The mass ratio values of added water were converted to volume by using 1.00 g/cm^3 for the density of water.

The $1/T_2$ vs. $1/f$ plots are meaningful only when constructed for the uppermost water layer, i.e. for the slowest relaxation (high T_2) domain. As seen in Fig. 8B, the $1/T_2$ vs. $1/f$ plots are linear, and thus, follow the theoretical equation derived by Simina et al.: [63]

$$\frac{1}{T_2} = \xi \frac{S}{V_0} \frac{1}{f^k} + \frac{1}{T_{2b}} \tag{6}$$

Here, ξ is the surface relaxation strength, S is the specific surface area and V_0 is the total pore volume. The value of the intercept, i.e. the bulk water relaxation rate was fixed at $1/T_{2b} = 0.45$ s^{-1}. The k exponent conveys information on the wettability of the surface and the saturation mechanism of the pores. As demonstrated by the linearity of the plots in Fig. 8B, the value of k is practically 1 for all hydrated aerogels. Overall, the $1/T_2$ vs. $1/f$ plots suggest that the total amount of surface water contributes to the fast relaxation domain. Thus, the filling of the pores of the aerogels is assumed to be a continuous process, which begins with the formation of a uniform, thick adsorption layer of water throughout the solid network. At higher water contents (filling factors), puddles appear in focal points of the network that form a quasi-bulk phase inside the pores. The $k = 1$ value suggests that there is a strong interaction between the homogeneous hydration layer and the puddles filling the pore interiors. Importantly, there are no spatially separated, preferred spots (e.g. inside micropores) for water accumulation. These assumptions are reasonable, since both silica and silica-gelatin are extremely hydrophilic matrices, [48] thus thermodynamic preferences dictate the continuous and homogeneous filling of the pores.

The normalized amplitudes of the fast and slow relaxation domains of water in the aerogels (cf. Fig. 8A) are given as function of water content in Fig. 8C. The amplitude of a domain is given by the size of its inverse Laplace peak, and normalized amplitude is calculated by dividing the amplitude with the sum of the amplitudes of the decays. As seen in Fig. 8C, the normalized amplitudes of the two domains are in close correlation with each other in every aerogel sample, especially at low water content (< 2.0 g/g). According earlier considerations, this can be attributed to a moderately fast exchange between the 2 relaxation domains of water in wet aerogels [62,66]. The amplitudes are more separated in the case of the hydrated silica-gelatin aerogels, meaning that water exchange is slower in these materials than in the hydrated silica aerogel, but it is still not in the slow exchange region. This correlation of the amplitudes strengthens the above described mechanistic theory: the pores of silica and silica-gelatin aerogels are filled by water in a continuous process which forms interconnected layers. As the water content increases, larger puddles form inside the pores, and water in these puddles exchange slower with the surface water layer.

One remarkable difference can be observed between the hydration mechanism of silica and silica-gelatin aerogels. The observed trend for the T_2 values of hydrated silica aerogel is typical for solid, hydrophilic mesoporous materials that retain their open pore

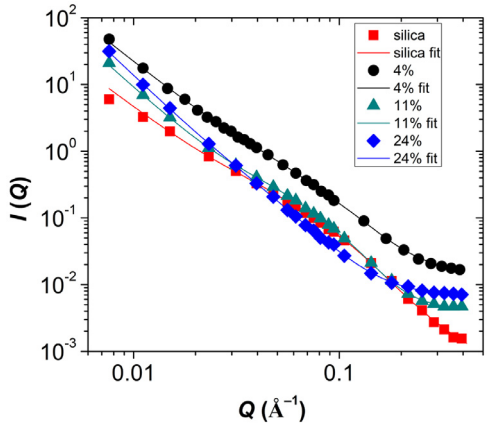

Fig. 9. Small angle neutron scattering (SANS) curves of silica and silica-gelatin hybrid aerogels completely filled with D_2O (3.3 g liquid / g aerogel). Solid lines represent data fitting to Beaucage model. Estimated structural parameters are given in Table 2.

structures, characteristic at their dry state, even when completely filled with water [65]. In contrast, there is an upward break in the trend of the T_2 relaxation times of silica-gelatin samples at around 2.0 g/g water content, as seen in Fig. 8A. At water contents lower than this threshold value, the wetting process of silica and silica-gelatin is practically the same, and can be attributed to the hydration of a hydrophilic mesoporous solid network. At high filling factors, the T_2 values steeply increase in silica-gelatin samples for both of the interchanging relaxation domains. This indicates that water is no longer bound to well-defined solid surfaces or confined in well-defined pores in these samples. Thus, it is reasonable to propose that at higher water content (>2.0 g/g), silica-gelatin matrices reach a critical level of hydration that induces the formation of hydrogel-like structures which is parallel to the extensive deformation of the hydrated aerogel backbone. This process is also well-expressed by the noted increase of the observed single self-diffusion coefficient of water by increasing water content in the case of the 24 wt.% gelatin aerogel (cf. Fig 7).

3.2.6. SANS of hydrated aerogels

The SANS scattering curves obtained for silica and silica-gelatin aerogels saturated with 3.3 g/g D_2O are shown in Fig. 9. These results represent the homogeneously hydrated (completely filled) states of the aerogels. No hydration microdomains were observed [86].

All scattering curves can be adequately fitted with the Beaucage model. The estimated R_g and p values are given in Table 2. The gyration radius slightly decreases upon the hydration of each aerogel, and p increases. The most obvious structural changes, compared to the dry state, can be observed above 11 wt.% gelatin. The scattering curve for the hydrated 24 wt.% gelatin hybrid contains information only in the Porod region meaning that the characteristic mesoporous network does not exist anymore in the sample. The value of the Porod exponent is highly above 4, which depicts a structure where the regions of different contrasts are separated by a gradient zone, instead of a sharp border. This is in-line with the structural information deduced from NMR diffusiometry and relaxometry. The pore network of the hybrid aerogel with the highest gelatin content collapses in water and forms a dense hydrogel-like matrix.

3.3. Summary of structural characterization

Results for dry aerogels by SANS, SEM and N_2 porosimetry are in good agreement with each another. All techniques suggest that the solid frameworks of the hybrid aerogels are somewhat looser and less barred than that of the parent silica aerogel. The contribution of the macropores to the porosity is higher, and the total mesopore volume decreases with increasing gelatin content. Contrast variation SANS experiments prove that silica-gelatin is hybridized on the molecular level in the solid backbones of the aerogels. Thus, gelatin does not form an outer “layer” on the inner pore walls, or shows any spatial preference in the matrix.

Nuclear magnetic resonance methods (NMR cryoporometry, diffusiometry and relaxometry) and SANS showed that the well-defined mesoporous structure of pristine silica aerogel is preserved when the material is immersed into water. The pore-structures of silica-gelatin hybrid aerogels significantly change upon hydration. At low gelatin content (4–11 wt.%), the structure is permeable and open, yet not as open, as it is in its dry state. Hybrid aerogels with high gelatin content (18–24 wt.%) show hydrogel-like characteristics in water, because their open pore structure collapses due to the extensive hydration of their backbones. A continuous, soft matrix forms from these hybrids. Gelatin content also governs the disintegration of the monolithic matrices. Aerogels of high gelatin content yield smaller microparticles in water, because the secondary forces between the protein molecules of the backbone are readily disrupted by hydration, in contrast to the limited hydrolysis of the covalent silica network.

3.4. Mechanism of drug release from aerogel carriers

3.4.1. Structure of active ingredient in aerogel

Silica and silica-gelatin aerogels were impregnated with ibuprofen and with ketoprofen by using the well-established technique of adsorptive precipitation in supercritical CO_2. The optimization of this technique for the impregnation of silica and silica-gelatin aerogel matrices has been carried out before [24,40,41].

The ibuprofen content of the loaded aerogels varies between 19 and 24 wt.%, and the ketoprofen content varies between 11 and 15 wt.% (Tables S1 and S2 in the Supporting Information). It is proved by XRD that the active ingredients are amorphous in the loaded aerogels. The spatial distribution of the active ingredient is homogeneous on the macroscopic level, as proved by FT-IR measurements. This was ensured by the constant stirring and the slow depressurization of the autoclave during adsorptive precipitation.

3.4.2. Design of drug release experiments

The loading of the drugs was realized by using dry, milled and sieved aerogel powders. These loaded aerogel particles were used in the release tests. The loaded aerogel particles spontaneously disintegrate in aqueous media to microparticles, eventually giving the characteristic size distributions, as seen in Fig. 4.

The detailed conditions of the drug release experiments and the solubilities of the amorphous forms of IBU and KET are given in Tables S1 and S2 in the Supporting Information. Sink conditions were fulfilled in the release experiments of both ibuprofen and ketoprofen in pH = 7.4 PBS, but not in pH = 2.0 HCl solution. At complete dissolution in HCl, the concentrations of IBU and KET are equivalent to ca. 80% and 40% of the respective solubilities. Representative release curves are shown in Figs. 10 and S3 for KET and in Fig. S4 for IBU (in the Supporting Information).

It should be noted for the profound evaluation of the drug release experiments, that both IBU and KET are amorphous in the aerogel carriers. In general, the amorphous forms of drugs have higher solubilities and dissolve faster than the crystalline forms [87–91]. Independent drug release experiments were performed in pH =2.0 HCl solution by using different weights of loaded aerogel and equal volume of release medium in each test. This ensures that the final drug concentration is different in each test. When drug release is given as the percentage of the total amount of loaded

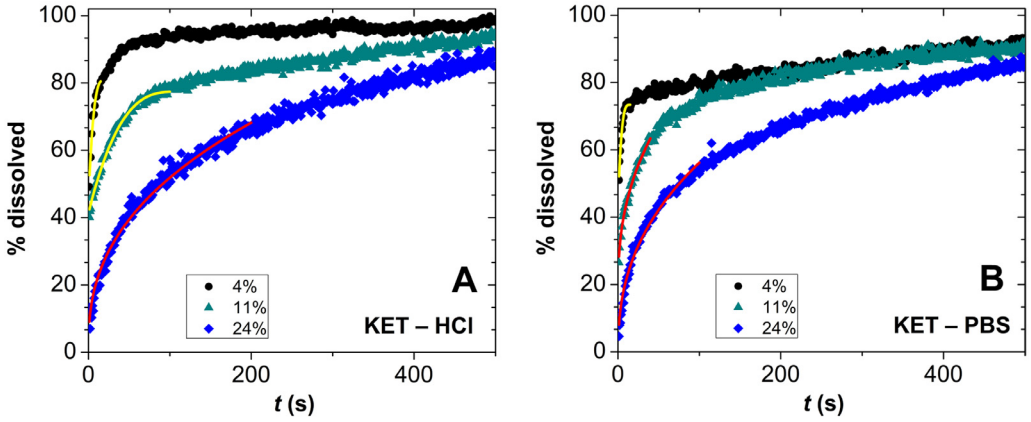

Fig. 10. Drug release experiments. The dissolution of ketoprofen from silica-gelatin hybrid aerogels containing 4–24 wt.% gelatin in pH = 2.0 HCl solution (A) and in pH = 7.4 PBS (B). Continuous lines represent model fitting: yellow – Hopfenberg, red – Peppas. Magnified versions of the same plots are given in Fig. S3 in the Supporting Information. Mass of loaded aerogel: 1.50 mg, volume of release medium: 3.0 mL, T = 37.0 °C, 300 rpm stirring. (For interpretation of the references to colour in this figure legend, the reader is referred to the web version of this article.)

drug, the independent release curves ideally overlap, as seen in Fig. S5 in the Supporting Information. This proves that the release of the amorphous IBU and KET is independent from the absolute concentration of the drug in the medium, even when sink conditions are not fulfilled, i.e. in HCl solution.

3.4.3. Evaluation of drug release experiments

The rate of drug release from the hybrid aerogel of the lowest gelatin content (4 wt.%) is one order of magnitude higher than the rate of drug release from the parent silica aerogel carrier. A possible explanation for this phenomenon has been proposed before [40]. In conclusion, the facile hydration and erosion of the 4 wt.% gelatin matrix is the key factor leading to the rapid desorption and dissolution of the drugs. Naturally, the rate of drug release depends on pH, because the strength of the interactions between the drug molecules and the pore walls is pH-dependent and changes with the charges (protonation states) of these [2,92]. Protonated molecules form hydrogen bonds, therefore their release is slower than that of the deprotonated species.

Interestingly, the kinetics of drug release displays an obvious correlation with the gelatin content of the hybrid aerogel carriers as seen in Figs. 10, S3 and S4. High gelatin content (11–24 wt.%) alters both the rate and the mechanism of drug release. The initial stage of release becomes significantly slower, and the overall shape of the kinetic curve reveals a diffusion controlled release mechanism. These characteristics are the most expressed in the case of the 24 wt.% gelatin carrier.

In order to confirm the qualitative mechanistic assumptions, the release curves were fitted to widely accepted semi-empirical release models [45,93]. Drug release curves in the case of the 4–11 wt.% gelatin aerogels can be successfully fitted by using the Hopfenberg model. The Hopfenberg model is a semi-empirical model used to describe drug leaching from eroding drug carriers where a zeroth order surface detachment is the limiting step of the release:

$$\frac{M_t}{M_{max}} = 1 - (1 - k_{obs1}t)^{n_1} \tag{7}$$

Here, M_t and M_{max} are the cumulative absolute amounts of drug released at time t and at infinite time, respectively. The observed rate constant is k_{obs1}, which depends on the initial concentration of drug in the system and on the physical dimensions of the carrier. Parameter n_1 is a shape factor representing the geometry of the carrier: spherical ($n_1 = 3$), cylindrical ($n_1 = 2$) or slab ($n_1 = 1$). The shape factor was fixed at $n_1 = 3$ for fitting release curves in the case of the aerogel carriers. The estimated kinetic parameters are given in Table S3 in the Supporting Information.

In the case of the aerogels of low-gelatin content, the kinetic curves start with a steep increase, i.e. burst release in the first 30 s (cf. Figs. S3 and S4). An initial burst, such as this, is characteristic for the release curves of erosion driven delivery systems.

On the other hand, it is natural to assume that gelatin forms a hydrogel in aqueous media, thus using it as a matrix component may lead to slower, diffusion controlled drug release. A versatile empirical model to describe diffusion controlled release of drugs is the Peppas model:

$$\frac{M_t}{M_{\max}} = k_{obs2}t^{n_2} \tag{8}$$

where M_t and M_{max} are the cumulative absolute amounts of drug released at time t and at infinite time, as defined previously. The observed rate constant is k_{obs2}, which incorporates the structural and geometric characteristics of the delivery system. Parameter n_2 is the release exponent and its value can be indicative of the mechanism of the limiting diffusion. The limiting value of the exponent changes with the geometry of the carrier vehicle and it also depends on the particle size distribution of the delivery system. Drug release curves measured in the case of the 18–24 wt.% gelatin hybrid aerogel carriers cannot be fitted by using the Hopfenberg model, but adequate fits were obtained by using the Peppas model at fixed $n_2 = 0.43$ value until ca. 65% cumulative release. (The limit of 65% is naturally set by the model itself, because the Peppas model is a short-time approximation.) [94,95]. The estimated kinetic parameters are given in Table S3 in the Supporting Information.

It is evident by examining the first 30 s of the experimental kinetic curves, that the erosion controlled initial burst release is also suppressed in the case of the high-gelatin hybrid aerogel carriers.

3.4.4. Mechanism of drug release

Molecular-level considerations on the mechanism of drug release from hybrid silica-gelatin aerogels can be drawn by correlating the results of the structural characterization of the wet carriers and the drug release kinetic results [1,3]. At low gelatin content (4–11 wt.%), an erosion controlled fast release process takes place, where the facile hydration of the matrix accelerates the desorption of the drug. The initial aerogel monoliths disintegrate to microparticles, and the adsorbed amorphous drug gets in contact with the release medium through the open pores. The strong interaction between the water molecules and the aerogel backbone repels the

adsorbed drug leading to its fast release, as further evidenced by the initial burst in the release curves [40,46]. Water hydrates the silica-gelatin backbone, but the gelatin content is too low for the formation of a dense hydrogel at 4–11 wt.% gelatin (cf. Section 3.3). The pores remain open and permeable for the drug molecules.

On the other hand, higher gelatin content (18–24 wt.%) significantly alters the release mechanism. In this case the disintegration of the particles also takes place, but now the gelatin content is sufficiently high for the formation of a continuous hydrogel in the presence of water, that practically entraps loaded molecules. Finally, the hindered diffusion of the drug through this hydrogel structure becomes the controlling factor that limits the release rate. The formation of the hydrogel also suppresses the initial burst release in the case of hybrid aerogels of high-gelatin content.

The liberation of active ingredient can be slightly altered by the protonation of the drug molecules in acidic media, where the protonated species form H-bonds with polar surface groups [2,92]. The kinetic curves recorded at pH = 7.4 stop at ca. 90% even at the long time-scale. This suggest that the thermodynamic-driven partitioning of the active ingredient between the carrier and the aqueous medium has an additional influence on drug release at pH = 7.4 [96].

4. Conclusions

Silica-gelatin aerogel based drug delivery systems developed in previous studies have now been investigated by an array of complementary physico-chemical characterization techniques. Such studies have not been performed before. The conclusions drawn from these materials chemistry related measurements are well-aligned with the quantitative drug release characteristics of the delivery systems in a wide range of composition.

Evidently, the release of the amorphous drugs from the aerogels shows a significant correlation with the composition of the hybrid aerogels. In addition, the composition of the hybrids governs their mechanism of wetting and hydration. Aerogels of low gelatin content (4–11wt%) are typical eroding carriers that rapidly release the loaded drugs, even show an initial burst. On the other hand, drug release is significantly slower from aerogels of high gelatin content (18–24 wt.%), and shows retarded characteristics. While all aerogels have approximately the same porosity and morphology in their dry state, and disintegrate into approximately the same sized and charged microparticles in water, the pore structures of these wet microparticles are radically different for the hybrids of different gelatin content. Namely, silica-gelatin aerogels of low gelatin content (4–11 wt.%) retain their open porous structure in water (similarly to the parent silica aerogel), but the pores of high-gelatin (18–24 wt.%) aerogels collapse due the facile hydration of the hybrid backbone, leading to a dense hydrogel structure. This continuous, soft hydrogel entraps loaded drug molecules, and thus, represents a diffusion barrier in drug release. Burst release is also suppressed in the case of hybrid aerogels of high gelatin content.

The burst release and the relatively high rate of additional drug release even at 24 wt.% gelatin content make this hybrid less competitive to achieve sustained release, than e.g., the preparation of coated aerogels [31,33]. Still, the simplicity and the versatility of the silica-gelatin aerogels are attractive.

The main point of the present study is to show that the shifting of the release mechanism from erosion facilitated to diffusion controlled in the case of the hybrid aerogels is the direct consequence of the hydration induced structural changes in the backbone in correlation with its gelatin content. A molecular-level explanation is given for the first time for the structure-activity relationship of a hybrid aerogel based drug delivery system. When considering the generalization of the above conclusions, it should be emphasized, that the above discussed characteristics are most probably valid only for inorganic-organic matrices that are hybridized on the molecular level. Importantly, contrast variation SANS experiments prove that this criterion is fulfilled for the present silica-gelatin aerogels. No spatial separation of gelatin, e.g. the formation of a “coating” takes place even on the molecular level in the porous aerogels.

Declaration of Competing Interest

The authors declare that they have no known competing financial interests or personal relationships that could have appeared to influence the work reported in this paper.

Acknowledgements

We are grateful to Andrea Szakács (University of Debrecen) and János Végh (University of Debrecen) for their technical assistance. J. Kalmár is grateful for the János Bolyai Research Scholarship of the Hungarian Academy of Sciences and for the New National Excellence Program (ÚNKP-19-4) of the Ministry of Innovation and Technology of Hungary for financial support. This research has been financially supported by the National Research, Development and Innovation Office, Hungarian Science Foundation (OTKA: FK_17-124571). The research was supported by the EU and co-financed by the European Regional Development Fund under the project GINOP-2.3.2-15-2016-00008.

Supplementary materials

Supplementary material associated with this article can be found, in the online version, at doi:10.1016/j.actbio.2020.01.016.

References

[1] A. Tzur-Balter, J.M. Young, L.M. Bonanno-Young, E. Segal, Mathematical modeling of drug release from nanostructured porous Si: combining carrier erosion and hindered drug diffusion for predicting release kinetics, Acta Biomater 9 (9) (2013) 8346–8353.
[2] D. Palmer, M. Levina, D. Douroumis, M. Maniruzzaman, D.J. Morgan, T.P. Farrell, A.R. Rajabi-Siahboomi, A. Nokhodchi, Mechanism of synergistic interactions and its influence on drug release from extended release matrices manufactured using binary mixtures of polyethylene oxide and sodium carboxymethylcellulose, Colloid. Surf. B 104 (2013) 174–180.
[3] T. Ukmar, U. Maver, O. Planinsek, V. Kaucic, M. Gaberscek, A. Godec, Understanding controlled drug release from mesoporous silicates: theory and experiment, J. Control. Release 155 (3) (2011) 409–417.
[4] V. Uskokovic, Mechanism of formation governs the mechanism of release of antibiotics from calcium phosphate nanopowders and cements in a drug-dependent manner, J. Mater. Chem. B 7 (25) (2019) 3982–3992.
[5] M.L. Parello, R. Rojas, C.E. Giacomelli, Dissolution kinetics and mechanism of Mg-Al layered double hydroxides: a simple approach to describe drug release in acid media, J. Colloid Interface Sci 351 (1) (2010) 134–139.
[6] T.J. Wooster, S. Acquistapace, C. Mettraux, L. Donato, B.L. Dekkers, Hierarchically structured phase separated biopolymer hydrogels create tailorable delayed burst release during gastrointestinal digestion, J. Colloid Interface Sci. 553 (2019) 308–319.
[7] C. Lopez-Iglesias, J. Barros, I. Ardao, F.J. Monteiro, C. Alvarez-Lorenzo, J.L. Gomez-Amoza, C.A. Garcia-Gonzalez, Vancomycin-loaded chitosan aerogel particles for chronic wound applications, Carbohydr. Polym. 204 (2019) 223–231.
[8] T. Budtova, Cellulose II aerogels: a review, Cellulose 26 (1) (2019) 81–121.
[9] P. Veres, D. Sebok, I. Dekany, P. Gurikov, I. Smirnova, I. Fabian, J. Kalmar, A redox strategy to tailor the release properties of Fe(III)-alginate aerogels for oral drug delivery, Carbohydr. Polym. 188 (2018) 159–167.
[10] S. Groult, T. Budtova, Tuning structure and properties of pectin aerogels, Eur. Polym. J 108 (2018) 250–261.
[11] C.A. García-González, C. López-Iglesias, A. Concheiro, C. Alvarez-Lorenzo, Biomedical applications of polysaccharide and protein based aerogels, Biobased Aerogels (2018) 295–323.
[12] K. Ganesan, T. Budtova, L. Ratke, P. Gurikov, V. Baudron, I. Preibisch, P. Niemeyer, I. Smirnova, B. Milow, Review on the production of polysaccharide aerogel particles, Materials 11 (11) (2018) 2144.
[13] C. Lopez-Iglesias, A.M. Casielles, A. Altay, R. Bettini, C. Alvarez-Lorenzo, C.A. Garcia-Gonzalez, From the printer to the lungs: inkjet-printed aerogel particles for pulmonary delivery, Chem. Eng. J. 357 (2019) 559–566.

[14] T. Athamneh, A. Amin, E. Benke, R. Ambrus, C.S. Leopold, P. Gurikov, I. Smirnova, Alginate and hybrid alginate-hyaluronic acid aerogel microspheres as potential carrier for pulmonary drug delivery, J. Supercrit. Fluid. 150 (2019) 49–55.
[15] T.A. Esquivel-Castro, M.C. Ibarra-Alonso, J. Oliva, A. Martinez-Luevanos, Porous aerogel and core/shell nanoparticles for controlled drug delivery: a review, Mater. Sci. Eng. C 96 (2019) 915–940.
[16] C.A. García-González, T. Budtova, L. Durães, C. Erkey, P. Del Gaudio, P. Gurikov, M. Koebel, F. Liebner, M. Neagu, I. Smirnova, An opinion paper on aerogels for biomedical and environmental applications, Molecules 24 (9) (2019) 1815.
[17] S. Zhao, W.J. Malfait, N. Guerrero-Alburquerque, M.M. Koebel, G. Nystrom, Biopolymer aerogels and foams: chemistry, properties, and applications, Angew. Chem. Int. Ed. 57 (26) (2018) 7580–7608.
[18] G. Vasvari, J. Kalmar, P. Veres, M. Vecsernyes, I. Bacskay, P. Feher, Z. Ujhelyi, A. Haimhoffer, A. Rusznyak, F. Fenyvesi, J. Varadi, Matrix systems for oral drug delivery: formulations and drug release, Drug. Discov. Today Technol. 27 (2018) 71–80.
[19] I. Smirnova, P. Gurikov, Aerogel production: current status, research directions, and future opportunities, J. Supercrit. Fluid. 134 (2018) 228–233.
[20] J. Stergar, U. Maver, Review of aerogel-based materials in biomedical applications, J. Sol.-Gel. Sci. Technol. 77 (3) (2016) 738–752.
[21] Z. Ulker, C. Erkey, An emerging platform for drug delivery: aerogel based systems, J. Control. Release 177 (2014) 51–63.
[22] S. Zhang, M. Xing, B. Li, Recent advances in musculoskeletal local drug delivery, Acta Biomater 93 (2019) 135–151.
[23] Ž. Knez, Z. Novak, M. Pantić, Incorporation of Drugs and metals into aerogels using supercritical fluids, Supercrit. Other High-Pressure Solvent Syst. (2018) 374–394.
[24] P. Gurikov, I. Smirnova, Amorphization of drugs by adsorptive precipitation from supercritical solutions: a review, J. Supercrit. Fluid. 132 (2018) 105–125.
[25] M. Pantic, Z. Knez, Z. Novak, Supercritical impregnation as a feasible technique for entrapment of fat-soluble vitamins into alginate aerogels, J. Non-Cryst. Solids 432 (2016) 519–526.
[26] W. Li-Hong, C. Xin, X. Hui, Z. Li-Li, H. Jing, Z. Mei-Juan, L. Jie, L. Yi, L. Jin-Wen, Z. Wei, C. Gang, A novel strategy to design sustained-release poorly water-soluble drug mesoporous silica microparticles based on supercritical fluid technique, Int. J. Pharm 454 (1) (2013) 135–142.
[27] M. Champeau, J.M. Thomassin, T. Tassaing, C. Jerome, Drug loading of polymer implants by supercritical CO_2 assisted impregnation: a review, J. Control. Release 209 (2015) 248–259.
[28] K. Matsuyama, N. Hayashi, M. Yokomizo, T. Kato, K. Ohara, T. Okuyama, Supercritical carbon dioxide-assisted drug loading and release from biocompatible porous metal–organic frameworks, J. Mater. Chem. B 2 (43) (2014) 7551–7558.
[29] I. De Marco, E. Reverchon, Starch aerogel loaded with poorly water-soluble vitamins through supercritical CO_2 adsorption, Chem. Eng. Res. Des. 119 (2017) 221–230.
[30] H. Maleki, L. Duraes, C.A. Garcia-Gonzalez, P. Del Gaudio, A. Portugal, M. Mahmoudi, Synthesis and biomedical applications of aerogels: possibilities and challenges, Adv. Colloid Interface Sci. 236 (2016) 1–27.
[31] C.A. Bugnone, S. Ronchetti, L. Manna, M. Banchero, An emulsification/internal setting technique for the preparation of coated and uncoated hybrid silica/alginate aerogel beads for controlled drug delivery, J. Supercrit. Fluid. 142 (2018) 1–9.
[32] Z. Ulker, C. Erkey, A novel hybrid material: an inorganic silica aerogel core encapsulated with a tunable organic alginate aerogel layer, RSC Adv. 4 (107) (2014) 62362–62366.
[33] M. Alnaief, S. Antonyuk, C.M. Hentzschel, C.S. Leopold, S. Heinrich, I. Smirnova, A novel process for coating of silica aerogel microspheres for controlled drug release applications, Micropor. Mesopor. Mat. 160 (2012) 167–173.
[34] H. Maleki, M.A. Shahbazi, S. Montes, S.H. Hosseini, M.R. Eskandari, S. Zaunschirm, T. Verwanger, S. Mathur, B. Milow, B. Krammer, N. Husing, Mechanically strong Silica-Silk fibroin Bioaerogel: a hybrid scaffold with ordered honeycomb micromorphology and multiscale porosity for bone regeneration, ACS Appl. Mater. Interfaces 11 (19) (2019) 17256–17269.
[35] H. Maleki, N. Huesing, Silica-silk fibroin hybrid (bio) aerogels: two-step versus one-step hybridization, J. Sol-Gel Sci. Technol (2019) 1–9.
[36] L. Goimil, M.E.M. Braga, A.M.A. Dias, J.L. Gomez-Amoza, A. Concheiro, C. Alvarez-Lorenzo, H.C. de Sousa, C.A. García-González, Supercritical processing of starch aerogels and aerogel-loaded poly (ε-caprolactone) scaffolds for sustained release of ketoprofen for bone regeneration, J. CO2 Util. 18 (2017) 237–249.
[37] V.S.S. Goncalves, P. Gurikov, J. Poejo, A.A. Matias, S. Heinrich, C.M.M. Duarte, I. Smirnova, Alginate-based hybrid aerogel microparticles for mucosal drug delivery, Eur. J. Pharm. Biopharm 107 (2016) 160–170.
[38] G. Nagy, G. Kiraly, P. Veres, I. Lazar, I. Fabian, G. Banfalvi, I. Juhasz, J. Kalmar, Controlled release of methotrexate from functionalized silica-gelatin aerogel microparticles applied against tumor cell growth, Int. J. Pharm 558 (2019) 396–403.
[39] P. Veres, G. Kiraly, G. Nagy, I. Lazar, I. Fabian, J. Kalmar, Biocompatible silica-gelatin hybrid aerogels covalently labeled with fluorescein, J. Non-Cryst. Solids 473 (2017) 17–25.
[40] P. Veres, M. Keri, I. Banyai, I. Lazar, I. Fabian, C. Domingo, J. Kalmar, Mechanism of drug release from silica-gelatin aerogel-Relationship between matrix structure and release kinetics, Colloid. Surface. B 152 (2017) 229–237.
[41] P. Veres, A.M. Lopez-Periago, I. Lazar, J. Saurina, C. Domingo, Hybrid aerogel preparations as drug delivery matrices for low water-solubility drugs, Int. J. Pharm 496 (2) (2015) 360–370.
[42] A.M. Zalfen, D. Nizet, C. Jerome, R. Jerome, F. Frankenne, J.M. Foidart, V. Maquet, F. Lecomte, P. Hubert, B. Evrard, Controlled release of drugs from multi–component biomaterials, Acta Biomater 4 (6) (2008) 1788–1796.
[43] S. Hajebi, N. Rabiee, M. Bagherzadeh, S. Ahmadi, M. Rabiee, H. Roghani-Mamaqani, M. Tahriri, L. Tayebi, M.R. Hamblin, Stimulus-responsive polymeric nanogels as smart drug delivery systems, Acta Biomater 92 (2019) 1–18.
[44] A. Gurikov, A. Kolnoochenko, M. Golubchikov, N. Menshutina, I. Smirnova, A synchronous cellular automaton model of mass transport in porous media, Comput. Chem. Eng. 84 (2016) 446–457.
[45] J. Siepmann, F. Siepmann, Modeling of diffusion controlled drug delivery, J. Control. Release 161 (2) (2012) 351–362.
[46] R. Mellaerts, E.J. Fayad, G. Van den Mooter, P. Augustijns, M. Rivallan, F. Thibault-Starzyk, J.A. Martens, In situ FT-IR investigation of etravirine speciation in pores of SBA-15 ordered mesoporous silica material upon contact with water, Mol. Pharm 10 (2) (2013) 567–573.
[47] J. Kalmar, M. Keri, Z. Erdei, I. Banyai, I. Lazar, G. Lente, I. Fabian, The pore network and the adsorption characteristics of mesoporous silica aerogel: adsorption kinetics on a timescale of seconds, RSC Adv. 5 (130) (2015) 107237–107246.
[48] M. Vorob'ev, Bound water measurements for aqueous protein solutions and food gels, Colloid. Surface. B 31 (1–4) (2003) 133–140.
[49] I. Lazar, I. Fabian, A continuous extraction and pumpless supercritical CO_2 drying system for laboratory-scale aerogel production, Gels 2 (4) (2016) 26.
[50] C. Ammann, P. Meier, A. Merbach, A simple multinuclear NMR thermometer, J. Magn. Reson. (1969) 46 (2) (1982) 319–321.
[51] O.V. Petrov, I. Furo, NMR cryoporometry: principles, applications and potential, Prog. Nucl. Magn. Res. Spect. 54 (2) (2009) 97–122.
[52] S.G. Allen, P.C.L. Stephenson, J.H. Strange, Internal surfaces of porous media studied by nuclear magnetic resonance cryoporometry, J. Chem. Phys. 108 (19) (1998) 8195–8198.
[53] N. Gopinathan, B. Yang, J.P. Lowe, K.J. Edler, S.P. Rigby, NMR cryoporometry characterisation studies of the relation between drug release profile and pore structural evolution of polymeric nanoparticles, Int. J. Pharm. 469 (1) (2014) 146–158.
[54] C.S. Johnson, Diffusion ordered nuclear magnetic resonance spectroscopy: principles and applications, Prog. Nucl. Mag. Res. Sp. 34 (3–4) (1999) 203–256.
[55] J. Götz, R. Hinrichs, Diffusion and relaxation in gels, Modern magnetic resonance, Springer (2008) 1713–1719.
[56] Y. Cohen, L. Avram, L. Frish, Diffusion nmr spectroscopy in supramolecular and combinatorial chemistry: an old parameter–new insights, Angew. Chem. Int. Ed. 44 (4) (2005) 520–554.
[57] C.H. Cho, Y.S. Hong, K. Kang, V.I. Volkov, V. Skirda, C.Y. Lee, C.H. Lee, Water self-diffusion in Chlorella sp. studied by pulse field gradient NMR, Magn. Reson. Imaging 21 (9) (2003) 1009–1017.
[58] R. Valiullin, V. Skirda, Time dependent self-diffusion coefficient of molecules in porous media, J. Chem. Phys. 114 (1) (2001) 452–458.
[59] T.J. Rottreau, C.M.A. Parlett, A.F. Lee, R. Evans, Diffusion NMR characterization of catalytic silica supports: a tortuous path, J. Phys. Chem. C 121 (30) (2017) 16250–16256.
[60] D. Benjamini, J.J. Elsner, M. Zilberman, U. Nevo, Pore size distribution of bioresorbable films using a 3-D diffusion NMR method, Acta Biomater 10 (6) (2014) 2762–2768.
[61] M. Holz, S.R. Heil, A. Sacco, Temperature-dependent self-diffusion coefficients of water and six selected molecular liquids for calibration in accurate 1H NMR PFG measurements, Phys. Chem. Chem. Phys. 2 (20) (2000) 4740–4742.
[62] I. Bardenhagen, W. Dreher, D. Fenske, A. Wittstock, M. Bäumer, Fluid distribution and pore wettability of monolithic carbon xerogels measured by 1H NMR relaxation, Carbon 68 (2014) 542–552.
[63] M. Simina, R. Nechifor, I. Ardelean, Saturation-dependent nuclear magnetic resonance relaxation of fluids confined inside porous media with micrometer-sized pores, Magn. Reson. Chem. 49 (6) (2011) 314–319.
[64] P.J. Barrie, Characterization of porous media using NMR methods, Annu. Rep. NMR Spectr. 41 (2000) 265–316.
[65] S.G. Allen, P.C.L. Stephenson, J.H. Strange, Morphology of porous media studied by nuclear magnetic resonance, J. Chem. Phys. 106 (18) (1997) 7802–7809.
[66] F. Vaca Chavez, E. Hellstrand, B. Halle, Hydrogen exchange and hydration dynamics in gelatin gels, J. Phys. Chem. B 110 (43) (2006) 21551–21559.
[67] T. Asakura, K. Isobe, S. Kametani, O.T. Ukpebor, M.C. Silverstein, G.S. Boutis, Characterization of water in hydrated Bombyx mori silk fibroin fiber and films by (2)H NMR relaxation and (13)C solid state NMR, Acta Biomater 50 (2017) 322–333.
[68] G. Beaucage, Approximations leading to a unified exponential power-law approach to small-angle scattering, J. Appl. Crystallogr. 28 (6) (1995) 717–728.
[69] P.W. Schmidt, Small-Angle scattering studies of disordered, porous and fractal systems, J. Appl. Crystallogr. 24 (5) (1991) 414–435.
[70] T. Ditroi, J. Kalmar, J.A. Pino-Chamorro, Z. Erdei, G. Lente, I. Fabian, Construction of a multipurpose photochemical reactor with on-line spectrophotometric detection, Photochem. Photobiol. Sci. 15 (4) (2016) 589–594.
[71] H. Liu, J.Y. Zhu, X.S. Chai, In situ, rapid, and temporally resolved measurements of cellulase adsorption onto lignocellulosic substrates by UV-vis spectrophotometry, Langmuir 27 (1) (2011) 272–278.

[72] Q.Q. Wang, J.Y. Zhu, C.G. Hunt, H.Y. Zhan, Kinetics of adsorption, desorption, and re-adsorption of a commercial endoglucanase in lignocellulosic suspensions, Biotechnol. Bioeng. 109 (8) (2012) 1965–1975.
[73] A. Forgacs, K. Moldovan, P. Herman, E. Baranyai, I. Fabian, G. Lente, J. Kalmar, Kinetic model for hydrolytic nucleation and growth of TiO2 nanoparticles, J. Phys. Chem. C 122 (33) (2018) 19161–19170.
[74] M. Thommes, K. Kaneko, A.V. Neimark, J.P. Olivier, F. Rodriguez-Reinoso, J. Rouquerol, K.S.W. Sing, Physisorption of gases, with special reference to the evaluation of surface area and pore size distribution (IUPAC Technical Report), Pure Appl. Chem. 87 (9–10) (2015) 1051–1069.
[75] C.J. Gommes, A.P. Roberts, Stochastic analysis of capillary condensation in disordered mesopores, Phys. Chem. Chem. Phys. 20 (19) (2018) 13646–13659.
[76] J.C. Dore, J.B.W. Webber, J.H. Strange, Characterisation of porous solids using small-angle scattering and NMR cryoporometry, Colloid. Surface. A 241 (1–3) (2004) 191–200.
[77] C.I. Merzbacher, J.G. Barker, K.E. Swider, D.R. Rolison, Effect of re-wetting on silica aerogel structure: a SANS study, J. Non-Cryst. Solids 224 (1) (1998) 92–96.
[78] J. Zaloga, A. Feoktystov, V.M. Garamus, W. Karawacka, A. Ioffe, T. Bruckel, R. Tietze, C. Alexiou, S. Lyer, Studies on the adsorption and desorption of mitoxantrone to lauric acid/albumin coated iron oxide nanoparticles, Colloid. Surface. B 161 (2018) 18–26.
[79] G.V. Franks, Zeta potentials and yield stresses of silica suspensions in concentrated monovalent electrolytes: isoelectric point shift and additional attraction, J. Colloid Interface Sci 249 (1) (2002) 44–51.
[80] D.J. Burgess, J.E. Carless, Microelectrophoretic studies of gelatin and acacia for the prediction of complex coacervation, J. Colloid Interface Sci 98 (1) (1984) 1–8.
[81] T.J. Rottreau, G.E. Parkes, M. Schirru, J.L. Harries, M.G. Mesa, P.D. Topham, R. Evans, NMR cryoporometry of polymers: cross-linking, porosity and the importance of probe liquid, Colloid. Surface. A 575 (2019) 256–263.
[82] M. Keri, Z. Nagy, L. Novak, E. Szarvas, L.P. Balogh, I. Banyai, Beware of phosphate: evidence of specific dendrimer-phosphate interactions, Phys. Chem. Chem. Phys. 19 (18) (2017) 11540–11548.
[83] M. Keri, C. Peng, X. Shi, I. Banyai, NMR characterization of PAMAM_G5.NH2 entrapped atomic and molecular assemblies, J. Phys. Chem. B 119 (7) (2015) 3312–3319.
[84] D. Noferini, A. Faraone, M. Rossi, E. Mamontov, E. Fratini, P. Baglioni, Disentangling polymer network and hydration water dynamics in polyhydroxyethyl methacrylate physical and chemical hydrogels, J. Phys. Chem. C 123 (31) (2019) 19183–19194.
[85] G. Vigil, Z. Xu, S. Steinberg, J. Israelachvili, Interactions of silica surfaces, J. Colloid Interface Sci 165 (2) (1994) 367–385.
[86] A. Luk, N.S. Murthy, W. Wang, R. Rojas, J. Kohn, Study of nanoscale structures in hydrated biomaterials using small-angle neutron scattering, Acta Biomater 8 (4) (2012) 1459–1468.
[87] S.Y. Lee, G. Yu, K. Shin, I.W. Kim, Estimating the solubility of amorphous ibuprofen using nanoporous anodic aluminum oxide as a solidification template, J. Nanosci. Nanotechno. 13 (3) (2013) 2348–2353.
[88] S. Mallick, S. Pattnaik, K. Swain, P.K. De, A. Saha, G. Ghoshal, A. Mondal, Formation of physically stable amorphous phase of ibuprofen by solid state milling with kaolin, Eur. J. Pharm. Biopharm. 68 (2) (2008) 346–351.
[89] S. Melzig, J.H. Finke, C. Schilde, A. Kwade, Formation of long-term stable amorphous ibuprofen nanoparticles via antisolvent melt precipitation (AMP), Eur. J. Pharm. Biopharm. 131 (2018) 224–231.
[90] S.C. Shen, W.K. Ng, L. Chia, Y.C. Dong, R.B. Tan, Stabilized amorphous state of ibuprofen by co-spray drying with mesoporous SBA-15 to enhance dissolution properties, J. Pharm. Sci. 99 (4) (2010) 1997–2007.
[91] N.J. Babu, A. Nangia, Solubility advantage of amorphous drugs and pharmaceutical Co-crystals, Cryst. Growth. Des. 11 (7) (2011) 2662–2679.
[92] X. Zhao, Z. Wang, A pH-sensitive microemulsion-filled gellan gum hydrogel encapsulated apigenin: characterization and in vitro release kinetics, Colloid. Surface. B 178 (2019) 245–252.
[93] J. Siepmann, F. Siepmann, Mathematical modeling of drug delivery, Int. J. Pharm. 364 (2) (2008) 328–343.
[94] P.L. Ritger, N.A. Peppas, A simple equation for description of solute release II. Fickian and anomalous release from swellable devices, J. Control. Release 5 (1) (1987) 37–42.
[95] P.L. Ritger, N.A. Peppas, A simple equation for description of solute release I. Fickian and non-fickian release from non-swellable devices in the form of slabs, spheres, cylinders or discs, J. Control. Release 5 (1) (1987) 23–36.
[96] A.V. Reis, M.R. Guilherme, A.F. Rubira, E.C. Muniz, Mathematical model for the prediction of the overall profile of in vitro solute release from polymer networks, J. Colloid Interface Sci 310 (1) (2007) 128–135.